# Nearly Self-Similar Pulse Compression in Horizontally Slotted Waveguides at 2.0 $\mu$m

Jiayao Huang ⬤, *Member, IEEE, Member, Optica*, Feng Ye ⬤, *Student Member, IEEE, Student Member, Optica*, and Qian Li ⬤, *Senior Member, IEEE, Senior Member, Optica*

*Abstract*—The picosecond pulse can be directly generated in the integrated mode-locked laser, which reduces the size of light source to the optical chip. However, it is still a challenge to directly generate femtosecond pulses in the integrated scheme. In this work, we theoretically propose nearly self-similar pulse compression in the silicon/silicon nitride horizontally slotted waveguides (Si-Si$_3$N$_4$ HSWs) that the femtosecond pulse can be acquired without assistance by active components. Our scheme consists of the single pulse compression, high-repetition-rate pulse train compression and two pulses combination and compression. For the single pulse compression, the input pulse can be compressed from 1 ps to 82.6 fs with a remarkable compression factor of 12.11. Moreover, we present a favorable approach of pulse parameter equations (PPEs), which provides the theoretical results in much shorter calculation time. Furthermore, we achieve the higher-peak-power pulse train compression and two pulses combination and compression in the same Si-Si$_3$N$_4$ HSWs, which accompanies with an impressive compression factor of 30.56 and 4.97. Eventually, self-similar pulse compression provides valid guidance for the integrated pulse compressor in the experimental endeavors.

*Index Terms*—Integrated optics, nonlinear optics, self-similar pulse compression, silicon photonics.

## I. INTRODUCTION

**C**HIP-SCALE ultrashort pulse generation has attracted intense attentions owing to their revolutionary applications in optical atomic clocks, spectroscopy, frequency conversion and optical computing [1], [2], [3], [4], [5]. Mode-locked lasers supplies a platform for generating the coherent and precisely spaced ultrashort pulses. Nevertheless, the integration of mode-locked lasers faces the challenges related to the typically low peak powers and limited controllability. Recently, Guo et al. illustrates an electrically pumped actively mode-locked lasers through hybrid integration with the III-V semiconductor optical amplifier, which produces near 4.8 ps output pulses with a repetition rate of 10 GHz [6]. Although gratifying progress have been achieved in the chip-scale mode-locked lasers, it is still a challenge to directly generate femtosecond pulses in the fully integrated

scheme. Thanks to the on-chip pulse compression schemes, the femtosecond pulse can be directly compressed from picosecond pulse, which are featured with stabilization, compactness and low energy consumption. A series of integrated platforms have been implemented to realize pulse compression, such as silicon (Si) [7], [8], silicon nitride (Si$_3$N$_4$) [9] and silicon rich nitride [10], [11]. Slot optical waveguides are essential components for integrated silicon photonic circuits, which spans a wide range of applications such as ultra-compact polarization beam splitter, biosensing, optical phased array chip and hybrid electro-optic modulator [12], [12], [13], [14], [15], [16]. Recently, numerous prominent foundries, including ST Microelectronics and AIM Photonics, have incorporated the Si$_3$N$_4$ layer integrated into the Si waveguide [17]. Si waveguide exhibits a strong nonlinear absorption effect, including two-photon absorption (TPA), free carrier absorption (FCA), and free carrier dispersion (FCD), which leads to the elevated power consumption. In contrast to Si waveguides, Si$_3$N$_4$ waveguides are not necessary to consider nonlinear absorption effect and exhibits lower propagation loss [18], [19], [20]. Hence, by combining the low-loss attributes of Si$_3$N$_4$ with the high refractive index feature of Si, it's feasible to improve the compression factor and peak power in the silicon/silicon nitride horizontally slotted waveguides (Si-Si$_3$N$_4$ HSWs).

Self-similar pulse compression has been widely reported to generate nearly chirp-free and pedestal-free femtosecond pulse in the fully integrated scheme, which provides the superiorities of reducing the compression length, nearly transform-limited characteristics and the ability to avoid pulse breakup even at high peak powers [21], [22], [23], [24], [25]. Self-similar pulse compression is beneficial to simultaneously realize pulse compression and spectral broadening in the single waveguide, since the nonlinearity is employed to generate new frequencies by the self-phase modulation, while the anomalous group-velocity dispersion (GVD) is utilized to preserve the balance of the soliton evolution [7]. In addition, realizing self-similar pulse compression is necessary to satisfy the condition of distributed gain $g(z) = g_0/(1-g_0 z)$ or exponentially varying dispersion $\beta_2(z) = \beta_{20}\exp(-z/z_0)$ [26]. To date, C. Mei et al. demonstrates a chalcogenide-silicon slot waveguide to obtain self-similar pulse compression with the compression factor of 12.3 [21]. Besides, mid-infrared self-similar pulse compression has been presented that the input pulse is compressed from 1 ps to 57.29 fs with the compression factor of 17.46 in a silicon ridge waveguide [22]. In our prior research, we introduced the tapered silicon waveguide
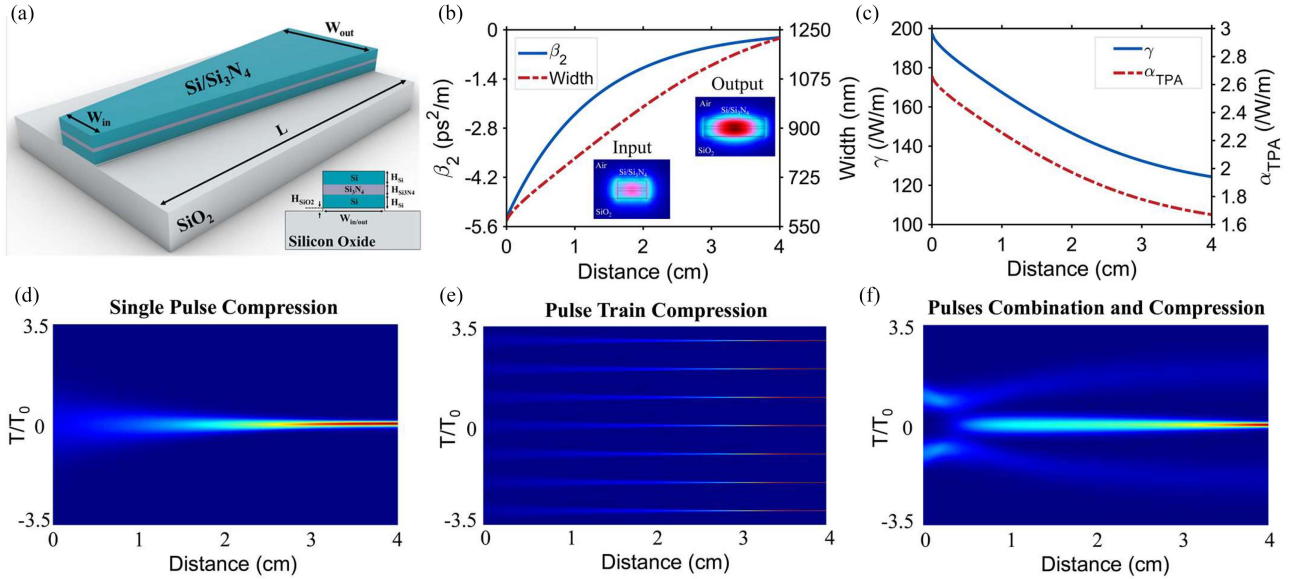
Fig. 1. The schematic depiction of nearly self-similar pulse compression characteristic in the Si-Si₃N₄ HSWs. (a) The proposed waveguide with the parameters represented as: waveguide width of the input and output segment ($W_{in}$ and $W_{out}$), silicon core height ($H_{Si}$), silicon nitride core height ($H_{Si_3N_4}$), silica layer height ($H_{SiO_2}$) and optimal waveguide length ($L$). The inset figure is the cross-section of the Si-Si₃N₄ HSWs, which is surrounded by air-cladding and buried oxide substrate. (b) Second-order dispersion ($\beta_2$) of the fundamental core mode and the waveguide width as a function of propagation distance. The inset electric-field distribution illustrates the mode patterns at the interfaces of the input and output waveguide. (c) Nonlinear coefficient ($\gamma$) and TPA loss coefficient ($\alpha_{TPA}$) curves along with propagation distance. (d-f) Nearly self-similar pulse compression schemes in the same Si-Si₃N₄ HSWs, including single pulse compression, high-repetition-rate pulse train compression and two pulses combination and compression.

for achieving self-similar pulse compression at the telecommunications wavelength [23]. Nonetheless, the substantial impact of TPA imposes limitations on both the compression factor and peak power. Compared with prior investigations, we employ silicon and silicon nitride materials, which offers the advantages in reducing nonlinear optical absorption effects and enhancing peak power. Additionally, in contrast to the strip waveguide, we utilize the horizontally slotted waveguide to provide flexibility in tailoring the second-order dispersion, which results in a broader range of adjustments. Furthermore, previous studies have primarily concentrated on designing a single waveguide structure to implement single pulse compression method. Our approach involves designing a single Si-Si₃N₄ HSWs to achieve three pulse compression methods of single pulse compression, high-repetition-rate pulse train compression and the two pulses combination and compression. The similar waveguide structure has been experimentally fabricated for the ultra-compact polarization beam splitter [12].

Here, as depicted in Fig. 1, we propose nearly self-similar pulse compression characteristics in the Si-Si₃N₄ HSWs. We can simultaneously realize nearly self-similar pulse compression with three conditions in the same Si-Si₃N₄ HSWs, which consists of single pulse compression, high-repetition-rate pulse train compression and two pulses combination and compression. Moreover, we compare the pulse evolution and compression performance in the different conditions. We further represent the numerical results of the pulse parameter equations, which can provide theoretical results of self-similar pulse compression. It is worth to mention that the calculation time from PPE is only 10% of directly solving the generalized nonlinear Schrödinger equation. The Si-Si₃N₄ HSWs works at the wavelength of

2.0 $\mu$m, since it is an attractive platform to achieve nonlinear frequency conversion toward the mid/far-IR spectral region. Besides, 2.0 $\mu$m fiber laser are mature and accessible, which exploits $Tm^{3+}$ and $Ho^{3+}$ doped gain material to supply laser emissions [27].

## II. THEORETICAL MODELS

In the numerical simulation, we adopt the generalized nonlinear Schrödinger equation (GNLSE) to model the pulse evolution at $\lambda_0 = 2.0\,\mu$m. Consideration of TPA is warranted in the wavelength range spanning from 0.85 $\mu$m to 2.2 $\mu$m [28]. In addition to TPA, FCA and FCD, we incorporate the influences of self-phase modulation (SPM), self-steepening (SS), and stimulated Raman scattering (SRS) [29], [30], [31],

$$
\frac{\partial A(z,t)}{\partial z}
$$

$$
= \sum_{k \geq 2} i^{k+1} \frac{\beta_k(z)}{k!} \frac{\partial^k A}{\partial t^k} - \frac{\alpha_c}{2}(1+i\mu)A - \frac{\alpha_0}{2}A
$$

$$
+ i\gamma \left(1 + \frac{i}{\omega_0}\frac{\partial}{\partial t}\right) \times \left(A \int_0^\infty R(t-t')\,|A(z,t')|^2\,dt'\right),
$$

$$(1)$$

where $A(z,t)$ represents the slowly varying pulse envelope of the electric field, $z$ is the direction of propagation and $t$ is the time in the pulses' frame of reference. $\alpha_0 = 0.2\,\mathrm{dB/cm}$ denotes the linear loss [32]. $\beta_k(z)$ signifies the $k$-th order dispersion. $\omega_0$ stands for the pulse center frequency, and $\gamma$ represents the nonlinearity coefficient. $\alpha_c = \sigma_c N_c$ characterizes the free carrier absorption loss, with $N_c$ denoting the free carrier density and

$\sigma_c = 2.41 \times 10^{-21}$ m$^2$ representing the free carrier absorption coefficient for silicon [33]. The parameter $\mu = 3.06$ signifies the free carrier dispersion [34]. Notably, the free carrier density $N_c$ is modeled according to [30],

$$\frac{\partial N_c(z,t)}{\partial t} = \frac{\beta_{TPA}}{2h\nu_0} \frac{|A(z,t)|^4}{A_{eff}^2} - \frac{N_c}{\tau_{eff}}, \tag{2}$$

$$A_{eff} = \frac{\left(\int\int_{-\infty}^{+\infty} |F(x,y)|^2 dxdy\right)^2}{\int\int_{-\infty}^{+\infty} |F(x,y)|^4 dxdy} \tag{3}$$

where $h\nu_0$ stands for the photon energy, $A_{eff}$ is the effective mode area and $\tau_{eff} = 3$ ns is the free carrier lifetime, respectively [35]. The nonlinear coefficient is assessed individually for each material within the Si-Si$_3$N$_4$ HSWs, which is scaled by corresponding fractional energy $E_{f,q}$ [36]. The effective nonlinear coefficient $\gamma$ can be represented as [36],

$$\gamma = \sum \gamma_q \cdot E_{f,q} + i\frac{\beta_{TPA}}{2A_{eff}}, \quad \gamma_q = \frac{2\pi n_2}{\lambda A_{eff}} \tag{4}$$

where $q$ denotes the materials of silicon, silica and silicon nitride, $\beta_{TPA} = 2.5 \times 10^{-12}$ m/W is the TPA coefficient of silicon, and the nonlinear coefficient $n_2$ of silicon, silica and silicon nitride are $1.1 \times 10^{-17}$ m$^2$/W, $4.7 \times 10^{-20}$ m$^2$/W and $2.4 \times 10^{-19}$ m$^2$/W [33], [34], [36], [37]. In addition, the nonlinear response function is expressed as [30],

$$R(t) = (1 - f_R)\delta(t) + f_R h_R(t), \tag{5}$$

where $h_R(t)$ is the Raman response function and $f_R = 0.043$. Note that the Raman term is not considered in (5) due to its relatively minor contribution in silicon nitride [38], [39], [40]. In preceding research, achieving self-similar pulse compression is strongly necessary to satisfy the decreasing exponentially GVD, which is described approximately below [23],

$$\beta_2(z) = \beta_{20}\exp(-\sigma z), \quad \sigma = \alpha_{20}\beta_{20} \tag{6}$$

where initial dispersion value $\beta_{20}$ is $-5.346$ ps$^2$/m, initial chirp coefficient $\alpha_{20}$ is $-14.93$ THz$^2$ and second-order dispersion decay rate $\sigma$ is $-79.8$ /m [23]. Typically, the pulse compression factor ($F_C$) serves as a metric to characterize the performance of compression, which is expressed as,

$$F_C = \text{FWHM}_{in}/\text{FWHM}_{out} \tag{7}$$

where FWHM$_{in}$ and FWHM$_{out}$ denotes the full width at half-maximum (FWHM) of the input and output pulses.

## III. Investigation on Nearly Self-Similar Pulse Compression in Horizontally Slotted Waveguides

### A. Modeling the Si-Si$_3$N$_4$ HSWs

From literature, the horizontally slotted waveguides are proposed to realize the excellent flat dispersion and provide more freedoms for waveguide dispersion engineering, which are widely exploited for the supercontinuum generation [41], [42], [43], [44]. To date, silicon and silicon nitride slot waveguides has been successfully employed in the polarization beam splitter and ultrafast pulse manipulation [12], [45]. Inspired by highly

nonlinear slot waveguides, we further propose the Si-Si$_3$N$_4$ HSWs in Fig. 1(a). The optical pulse can partly propagate in the silicon nitride slot layer, which proves beneficial in mitigating the influence of two photon absorption, consequently enhancing pulse compression performance. Crucially, the Si-Si$_3$N$_4$ HSWs amalgamates the superiorities of conventional silicon waveguides and silicon nitride waveguides, such as high refractive index contrast, large nonlinearity, strong confinement and optimized dispersion properties. Recently, Si$_3$N$_4$ have been experimentally integrated in the Si photonic platforms, as evidenced by demonstrations in the photonic integrated circuits, optical phased array chip and ultra-compact polarization beam splitter [12], [15], [17], [18]. Here, to realize nearly self-similar pulse compression, we introduce the Si-Si$_3$N$_4$ HSWs in Fig. 1(a), which can be manufactured using CMOS technology [43]. The structure consists of two 150 nm thick Si layers and a 50 nm thick Si$_3$N$_4$ slot layer, where the Si and Si$_3$N$_4$ can be deposited above a 2 mm buried oxide layer using a low pressure chemical vapor deposition (LPCVD) process [46]. In the next step, the positive electron beam resist is applied to spin-coating on the substrate. Subsequently, the resist can be patterned using electron beam lithography (EBL) [12]. Eventually, reactive ion etching (RIE) is employed to etch the Si layer and Si$_3$N$_4$ slot layer to produce the Si-Si$_3$N$_4$ HSWs. Our device offers considerable flexibility for dispersion engineering, with the geometric parameters fully optimized as $H_{Si} = 150$ nm, $H_{Si_3N_4} = 50$ nm, $H_{SiO_2} = 10$ nm, $L = 4$ cm, $W_{in} = 570$ nm and $W_{out} = 1220$ nm. We have considered the Sellmeier's equations of the silicon, silicon nitride and silica materials in the simulation. The wavelength-dependent material index of silicon and silica can be expressed as [47], [48], [49],

$$n_{Si}^2(\lambda) = \varepsilon_{Si} + \frac{C_1}{\lambda^2} + \frac{C_2\lambda^2}{\lambda^2 - \lambda_2^2} \tag{8}$$

$$n_{SiO_2}^2(\lambda) = 1 + \frac{C_3\lambda^2}{\lambda^2 - \lambda_3^2} + \frac{C_4\lambda^2}{\lambda^2 - \lambda_4^2} + \frac{C_5\lambda^2}{\lambda^2 - \lambda_5^2} \tag{9}$$

where $\varepsilon = 11.6858$, $C_1 = 0.939816$ $\mu$m$^2$, $C_2 = 0.00810461$, $\lambda_2 = 1.1071$ $\mu$m, $C_3 = 0.6961663$, $\lambda_3 = 0.0684043$ $\mu$m, $C_4 = 0.4079426$, $\lambda_4 = 0.1162414$ $\mu$m, $C_5 = 0.8974794$, $\lambda_5 = 9.896161$ $\mu$m and the wavelength $\lambda$ is in units of micrometer. The Sellmeier's equation of silicon nitride is given as [50],

$$n_{Si_3N_4}^2(\lambda) = 1 + \frac{C_6\lambda^2}{\lambda^2 - \lambda_6^2} + \frac{C_7\lambda^2}{\lambda^2 - \lambda_7^2} \tag{10}$$

where $C_6 = 3.0249$, $\lambda_6 = 135.3406$ nm, $C_7 = 40314$, $\lambda_7 = 1239842$ nm and the wavelength $\lambda$ is in units of nanometer. As depicted in Fig. 1(b), the tapered profile width and the second-order dispersion ($\beta_2$) curves are illustrated along with the propagation distance, indicating their capability to achieve nearly self-similar pulse compression. $\beta_2$ is exponentially decreased from $-5.346$ ps$^2$/m to $-0.22$ ps$^2$/m, which are calculated by finite element method based on the fundamental core mode. The waveguide width exhibits a nearly linear increasing from 570 nm to 1220 nm along with the popagating direction. Thanks to the waveguide fabrication techniques [32], [36], [43],

TABLE I
PARAMETERS EMPLOYED FOR ESTIMATING THE EFFECTIVE NONLINEAR
COEFFICIENT OF THE Si-Si$_3$N$_4$ HSWs AT $\lambda_0 = 2.0\ \mu m$

| Material | $n$ | $n_2$ (m$^2$/W) | $A_{\text{eff}}$ ($\mu$m$^2$) |
|---|---|---|---|
| Si | 3.45 | $1.1 \times 10^{-17}$ | 0.144 |
| Si$_3$N$_4$ | 1.98 | $2.4 \times 10^{-19}$ | 0.0258 |
| SiO$_2$ | 1.44 | $4.7 \times 10^{-20}$ | 0.148 |

it becomes feasible to produce the suggested Si-Si$_3$N$_4$ HSWs with a high-precision CMOS facility. We present all parameters for estimating the effective nonlinear coefficient of the HSWs at $\lambda_0 = 2.0\ \mu m$, which are denoted in the Table I [33], [34], [36], [37]. In Fig. 1(c), the evolution of the estimated $\gamma$ and $\alpha_{\text{TPA}}$ along with varying popagating distance is calculated by the (4) and (5), where $\gamma$ reduces from 196.70 /W/m to 124.37 /W/m and $\alpha_{\text{TPA}}$ declines from 2.65 /W/m to 1.67 /W/m. It is seen that $\gamma$ shares an approaching trend with $\alpha_{\text{TPA}}$, which are both monotonically decreasing.

Next, we employ the proposed Si-Si$_3$N$_4$ HSWs to realize nearly self-similar pulse compression in Fig. 1(d)–1(f), which includes single pulse compression, high-repetition-rate pulse train compression and two pulses combination and compression. The temporal evolutions of nearly self-similar pulse compression are demonstrated in Fig. 1(d), which contains all higher-order dispersion terms, higher-order nonlinearity and absorption loss. The optical pulse is gradually compressed and the pulse energy is concentrated to the center of the pulse, where the compression factor reaches up to 12.11 and the pedestal energy is close to zero. Furthermore, Fig. 1(e) illustrates the nearly self-similar pulse compression of high-repetition-rate pulse train, which comprises both pulse shaping and pulse compression. Ultimately, the input pulse train undergoes temporal compression with the compression factor of 30.56. As shown in Fig. 1(f), two pulses combination and compression encompass three stages of rapid combination, steady adjustment, and nearly self-similar pulse compression. Moreover, two raised cosine pulses are initially merged into a single combined pulse, followed by the realization of nearly self-similar compression with a compression factor of 4.97.

### B. Numerical Results and Discussion of Self-Similar Pulse Compression in the Si-Si$_3$N$_4$ HSWs At 2.0 $\mu$m

We chose the chirped fundamental soliton pulse to study the self-similar pulse compression in the Si-Si$_3$N$_4$ HSWs at 2.0 $\mu$m,

$$A(0, t) = \sqrt{P_0}\,\text{sech}\,(t/T_0)\exp\left(i\alpha_{20}t^2/2\right), \qquad (11)$$

where $T_0$ stands for the initial pulse width of 567.3 fs which corresponds to the FWHM of 1 ps. $P_0$ is the initial peak power of 0.085 W ($P_0 = |\beta_{20}|/\gamma_0/T_0^2$). In Fig. 2(a), the pulse is compressed from 1 ps to 82.6 fs, which results in a notable pulse compression factor of 12.11. The corresponding pulse peak power enhances from 0.085 W to 0.82 W in the temporal field, where the ultimate peak power attains 9.71 times higher than the initial input peak power. Simultaneously, Fig. 2(b) illustrates the normalized spectrum distributions that the chirped fundamental
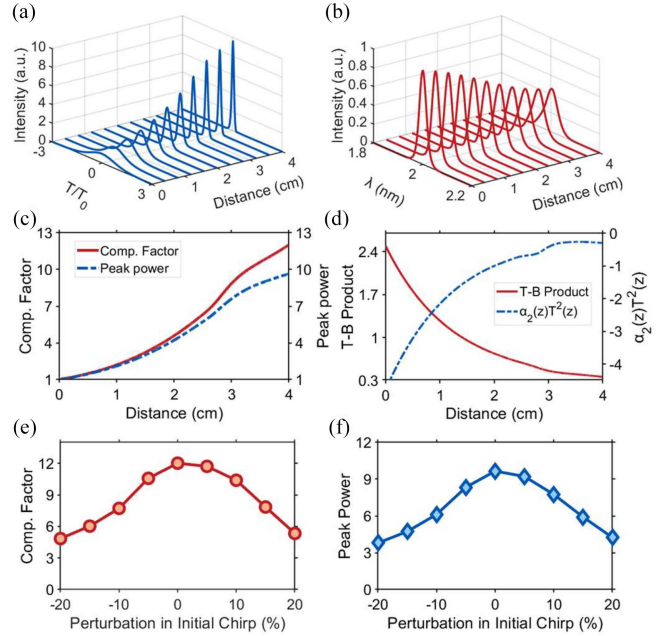


Fig. 2. 3D plots of the pulse (a) temporal and (b) spectrum field along the propagating direction. Corresponding simulated evolution of (c) the compression factor and peak power (d) time-bandwidth product and normalized chirp during propagation of the hyperbolic secant pulse. (e) The compression factor and (f) the pedestal energy versus the perturbation in initial chirp from $-20\%$ to $+20\%$.

soliton propagates in the anomalous dispersion region and experiences the spectral broadening. Additionally, we observe that the temporal and spectrum profile still maintain superior symmetry without any pedestal or satellite peaks. As the propagation distance increases in Fig. 2(c) and (d), the compression factor and peak power of the soliton are monotonically enhanced, while the time-bandwidth product (T-B Product) and the normalized chirp are obviously declined. In Fig. 2(c), although the upward trends of compression factor and peak power are similar, the output peak power is comparatively reduced since the energy loss is induced by TPA and a portion of the energy is utilized for electronic transitions to higher energy states [28]. As shown in Fig. 2(d), the time-bandwidth product is generally approaching 0.315 which is the constant associated with transform-limited hyperbolic secant pulses [51]. The termination point of the time-bandwidth product is 0.359, which indicates the output pulse remains undistorted and maintains the characteristics of hyperbolic secant pulses. In addition, the evolution of the normalized chirp $C(z) = \alpha_2(z)T^2(z)$ is demonstrated in Fig. 2(d), which is calculated by the polynomial fit of the pulse phase. It's important to highlight that the accumulation of higher-order dispersion, higher-order nonlinearity and absorption loss lead to the reduction of the compression factor and peak power in Fig. 2(c), and this cumulative impact is also responsible for a significant fluctuation in the normalized chirp in Fig. 2(d). As illustrated in Fig. 2(e), the perturbation in the initial chirp from $-20\%$ to $20\%$ has a slight influence on the compression factor, ranging from 4.85 to 12.11. In Fig. 2(f), the peak power exhibits a similar trend to the compression factor, ranging from 3.79

to 9.71. It's worth noting that the curves of the compression factor and peak power exhibit symmetry with the perturbation in initial chirp from $-20\%$ to $20\%$. This demonstrates that both increasing and decreasing chirp have the same effect on the pulse compression.

We have a couple of approaches to explore self-similar pulse compression in the Si-Si$_3$N$_4$ HSWs. One method involves directly using numerical methods to simulate the GNLSE. Alternatively, we can utilize semi-analytical reduction techniques like the Lagrangian Variational Method (LVM) [52] or the Projection Operator Method (POM) [53], [54] to derive the pulse parameter equations (PPEs) of the pulse evolution. By employing the Lagrangian of the GNLSE and choosing the suitable ansatz function of the hyperbolic secant, we can derive the ordinary differential equations (ODEs) to govern the parameters of the ansatz in the LVM. In addition, the numerical solutions of the ODEs have the capability to forecast the evolution of the pulse parameters [55]. In our calculation, we demonstrate the primary steps to express the GNLSE in terms of pulse parameter equations, which utilizes the perturbed Lagrangian approach. We firstly provide the general pulse parameter equations of the hyperbolic secant ansatz, and we insert this ansatz function into the Lagrangian of the GNLSE. Upon evaluating the integral, we can obtain the expression involving the derivatives of the pulse parameters. Here, the GNLSE is considered in the form of,

$$A_z + \frac{i\beta_2(z)}{2}A_{tt} - i\left(\sum \gamma_q \cdot E_{f,q}\right)|A|^2 A = \varepsilon R \quad (12)$$

where

$$\varepsilon R = -\alpha_{\text{TPA}}|A|^2 A - \frac{\alpha_0}{2}A + \frac{\beta_3(z)}{6}A_{ttt} - \frac{\alpha_c}{2}(1 + i\mu)A$$
$$- iT_R\left(\sum \gamma_q \cdot E_{f,q}\right)A\left(|A|^2\right)_t$$
$$- \frac{\sum \gamma_q \cdot E_{f,q}}{\omega_0}\left(|A|^2 A\right)_t, \quad (13)$$

where $A_z$ is the slowly varying envelope of the axial electrical field, $\beta_2(z)$ and $\sum \gamma_q \cdot E_{f,q}$ represent the GVD and SPM, respectively. These definitions of the variables and parameters are for the context of envelope soliton propagation in the Si-Si$_3$N$_4$ HSWs. $\varepsilon R$ represents the perturbation term of TPA, linear loss, third-order dispersion, FCA, FCD, SS and SRS. A typical value of $T_R = 4$ fs (at the wavelength near 2.0 $\mu$m) is employed in this section. The Lagrangian for (12) without the perturbation term ($\varepsilon R = 0$) is expressed as,

$$L = \int_{-\infty}^{\infty}\left[\frac{\beta_2(z)}{2}|A_t|^2 + \frac{\sum \gamma_q \cdot E_{f,q}}{2}|A|^4\right.$$
$$\left. + \frac{i}{2}\left(A^* A_z - AA_z^*\right)\right]dt \quad (14)$$

We study the hyperbolic-secant ansatz function provided by,

$$f = x_1 \text{sech}\left(\frac{t - x_2}{x_3}\right)$$
$$\exp\left[\frac{ix_4(t - x_2)^2}{2} + ix_5(t - x_2) + ix_6\right], \quad (15)$$

where $x_1, x_2, x_3, x_4, x_5$ and $x_6$ stand for the pulse amplitude, temporal position, width, chirp, frequency and phase. The variational equations are given by [56],

$$\frac{\partial L}{\partial x_j} - \frac{d}{dz}\left(\frac{\partial L}{\partial \dot{x}_j}\right) = \int_{-\infty}^{\infty}\varepsilon R \frac{\partial f_z^*}{\partial \dot{x}_j} \quad j = 1, 2, \ldots, 6, \quad (16)$$

where $\dot{x}_j$ is denoted as $dx_j/dz$. By substituting the ansatz function $f$ into $\varepsilon R$ (setting $A = f$ in (13)) and integrating the right-hand side of (16), we obtain the collective variable equations as,

$$\frac{dx_1}{dz} = \frac{\beta_2(z)x_1 x_4}{2} - \frac{\beta_3(z)x_1 x_4 x_5}{2} - \frac{\alpha_0 x_1}{2} - \frac{\alpha_c x_1}{2}$$
$$- \frac{2\alpha_{TPA}x_1^3}{3} - \frac{2\alpha_{TPA}x_1^3}{\pi^2}, \quad (17)$$

$$\frac{dx_2}{dz} = -\beta_2(z)x_5 + \beta_3(z)\left(\frac{1}{6x_3^2} + \frac{\pi^2 x_3^2 x_4^2}{24} + \frac{x_5^2}{2}\right)$$
$$+ \frac{\left(\sum \gamma_q \cdot E_{f,q}\right)x_1^2}{\omega_0}, \quad (18)$$

$$\frac{dx_3}{dz} = -\beta_2(z)x_3 x_4 + \beta_3(z)x_3 x_4 x_5 + \frac{4\alpha_{TPA}x_1^2 x_3}{\pi^2}, \quad (19)$$

$$\frac{dx_4}{dz} = \beta_2(z)\left(x_4^2 - \frac{4}{\pi^2 x_3^4}\right) + \beta_3(z)\left(\frac{4x_5}{\pi^2 x_3^4} - x_4^2 x_5\right)$$
$$+ \left(\sum \gamma_q \cdot E_{f,q}\right)\left(-\frac{4x_1^2}{\pi^2 x_3^2} + \frac{4x_1^2 x_5}{\omega_0 \pi^2 x_3^2}\right), \quad (20)$$

$$\frac{dx_5}{dz} = \frac{2\left(\sum \gamma_q \cdot E_{f,q}\right)x_1^2 x_4}{3\omega_0} + \frac{8T_R x_1^2}{15x_3^2}, \quad (21)$$

$$\frac{dx_6}{dz} = \beta_2(z)\left(\frac{1}{3x_3^2} - \frac{x_5^2}{2}\right)$$
$$+ \beta_3(z)\left(-\frac{x_5}{6x_3^2} + \frac{\pi^2 x_3^2 x_4^2 x_5}{24} + \frac{x_5^3}{3}\right)$$
$$+ \left(\sum \gamma_q \cdot E_{f,q}\right)\left(\frac{5x_1^2}{6} + \frac{x_1^2 x_5}{6\omega_0}\right) - \frac{\alpha_c \mu}{2}, \quad (22)$$

As depicted in Fig. 3(a), the compression factor and peak power profiles are calculated from GNLSE and PPEs, which shares a similar trend and exhibits a monotonic increasing along with the propagating direction. It can be observed that the pulse width of GNLSE declines from 1 ps to 82.6 fs with the compression factor of 12.11, while the pulse width of PPEs drastically drops down from 1 ps to 76.80 fs with the compression factor of 13.02. This phenomenon is contributed from the higher-order nonlinear effects, which causes that the pulse undergoes a certain deformation in the GNLSE. However, the pulse transmission computed by PPEs is not necessary to consider the pulse distortion since the output pulse is strictly based on hyperbolic-secant ansatz function [23]. Fig. 3(b) illustrates the normalized chirp comparison between GNLSE and PPEs, which nearly remains the same as the soliton propagating. Fig. 3(c) and (d) indicates the temporal observations of self-similar pulse compression dynamics in the linear scales and logarithmic scales, which
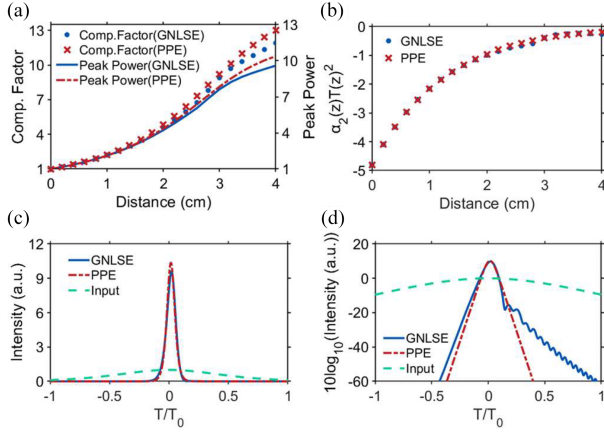
Fig. 3. Self-similar pulse compression characteristics from GNLSE results and PPEs results. (a) Evolution of the compression factor and peak power from the precise solution. (b) Evolution of the normalized chirp parameter. Input temporal, output temporal through GNLSE results and output PPE results in (c) linear scales and (d) logarithmic scales.

TABLE II
PULSE COMPRESSION PERFORMANCE OF GNLSE AND PPEs IN FIG. 3

| Method | Pulse Width (fs) | Compression Factor | Peak power (a.u.) |
|--------|------------------|--------------------|--------------------|
| GNLSE | 82.60 | 12.11 | 9.71 |
| PPEs | 76.80 | 13.02 | 10.38 |

exhibits a high degree of similarity in the calculation results from GNLSE and PPEs. In Fig. 3(c), the compressed pulse maintains practical symmetry on both sides and overall preserves a hyperbolic secant pulse shape. As shown in Fig. 3(d), the pulse profile of the PPEs maintains standard sech shape, however the output pulse of the GNLSE displays a noticeable tailing effect which is attributed to the influence of higher-order dispersion.

The comparison results of output pulse width, compression factor and the output normalized peak power between GNLSE and PPEs is presented in Table II. The GNLSE offers the advantages of accommodating diverse nonlinear effects and observing the pulse distortion. Nonetheless, it is worth noting that GNLSE computations can be time-consuming, which poses a challenge for evaluating the pulse compression results in a short time. PPEs primarily provides the mathematical expressions adaptable to the interest pulse shape such as hyperbolic secant pulse. Notably, PPEs boasts the advantage of swiftly obtaining calculation results, and the calculation time from PPE is only 10% of directly solving the GNLSE. Hence, the PPEs is more efficient and the GNLSE is more precise.

## C. Nearly Self-Similar Pulse Compression of High-Repetition-Rate Pulse Train in the Si-Si₃N₄ HSWs

The initial raised cosine optical pulse train with the initial chirp can be represented as [57],

$$A(0,t) = \sum_{n=-N}^{N} \sqrt{P_0} \cos(\pi t/T_0) \exp\left(i\alpha_{20}(t-nT_0)^2/2\right),$$
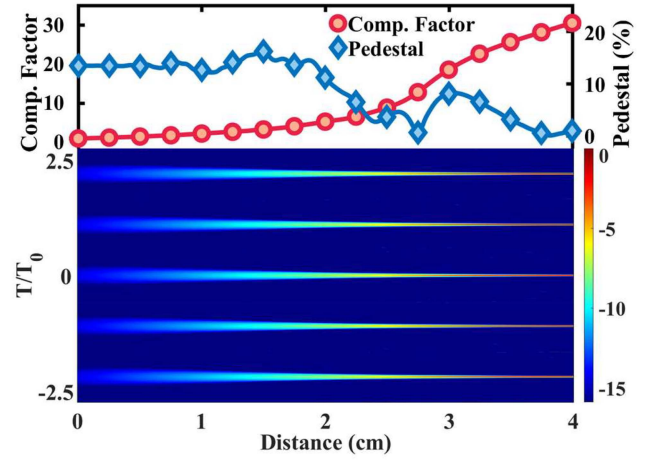$$t/T_0 \in [(n-0.5), (n+0.5)], \tag{23}$$



Fig. 4. Evolutions of the pulse compression factor, pedestal energy and temporal field of the optical pulse in the high-repetition-rate pulse train compression dynamics. For clarity, only five pulses are plotted.

where the initial pulse width $T_0$ is 4.4 ps (corresponding to 228 GHz) and the FWHM of a single pulse is 2.2 ps. The initial peak power is 0.0369 W ($P_0 = 8\pi^2|\beta_{20}|/T_0^2/\gamma_0/3$). The number of pulses in the pulse train is selected as 31 with $N = 15$ for the simulation. Fig. 4 reveals a comprehensive simulation for the high-repetition-rate pulse train compression dynamics, which employs the intensity contour plots and line charts to depict temporal field, compression factor and the pedestal energy evolution. In the intensity contour plots, the optical pulse undergoes pulse shaping and pulse compression, which initially transforms from the raised cosine pulse to the hyperbolic secant pulse and eventually realizes nearly self-similar pulse compression. The line charts illustrate a monotonic enhancement in the compression factor. Notably, the pedestal energy approaches to zero as the soliton propagates to 2.6 cm, which is a key point to indicate that the raised cosine pulses have been transformed into the hyperbolic secant pulses. Furthermore, the shaped sech pulses undergo nearly self-similar compression, which the compression factor eventually reaches up to 30.56 accompanied with the pedestal energy of 0.9%.

To illustrate the soliton characterization, as shown in Fig. 5, we present the temporal and spectrum profiles of five input pulses and output compressed pulses from the pulse train. In Fig. 5(a), the input pulse train experiences temporal compression and ultimately transforms into a higher-peak-power output pulse train, which the input pulses can be compressed from 2.2 ps to 72 fs with the compression factor of 30.56. It is important to note that the output pulse train exhibits clear separation, and the mutual interactions between pulses have been successfully eliminated. Each individual pulse in the compressed pulse train shares the same peak power and pulse duration. In Fig. 5(b), the input and output temporal profiles are presented in logarithmic scale, where the pulse shape undergoes a noticeable evolution that the raised cosine shape transforms to nearly hyperbolic-secant shape. In Fig. 5(c), both the shaped sech pulse and the output compressed pulse are approximately remaining the same with their fitted hyperbolic secant pulses. This calculated result
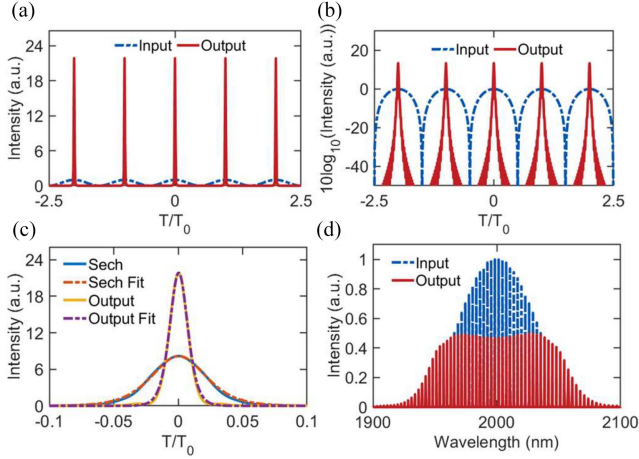
Fig. 5. Temporal profile of five input pulse (dashed line) and five output compressed pulse (solid lines) in (a) linear and (b) logarithmic scales. (c) The shaped sech pulse and the output compressed pulse compared with their fitted hyperbolic secant pulses. (d) Spectral profile of the input and output pulse.
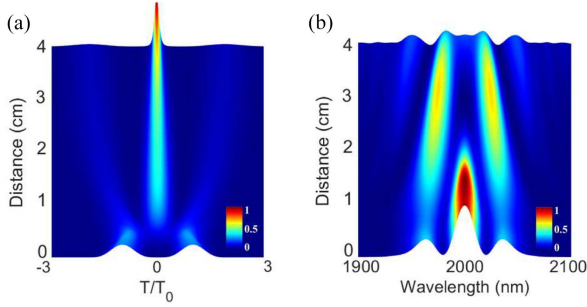


Fig. 6. The evolution of temporal and spectral characteristics for the two pulses combination and compression, which consists of rapid combination, steady adjustment and nearly self-similar pulse compression.

highlights that the Si-Si$_3$N$_4$ HSWs serves an additional function of pulse shaping that the initial raised cosine optical pulse train transforms to the hyperbolic secant pulse train. Fig. 5(d) indicates the normalized spectrum distributions of the optical intensity, which can be observed that the compressed pulse train experiences the spectral broadening and the final spectrum still maintains symmetry under the influence of strong SPM effect.

### D. Simultaneous Two Pulses Combination and Nearly Self-Similar Pulse Compression in the Si-Si$_3$N$_4$ HSWs

In order to study two pulses combination and compression, we utilize two chirped RC pulses which is denoted as [25], [58],

$$\frac{\sqrt{P_0}}{2} \left\{ 1 + \cos\left[\pi\left(t/T_0 + 1\right)\right] \right\} \exp\left(i\alpha_{20}t^2/2\right), t/T_0 \in [-2, 2],$$
(24)

where $T_0$ and $P_0$ stand for the initial pulse width and initial peak power ($P_0 = 2.5|\beta_{20}|/\gamma/T_0^2$). The other pulse parameters are chosen as $P_0 = 0.90$ W and $T_0 = 274.8$ fs with the FWHM of 200 fs. In contrast to the high-repetition-rate pulse train compression with the separate initial linear chirps in Fig. 4, the input pulses share the same linear chirp in Fig. 6. It can be assumed that a number of low repetitive rate pulses with the same
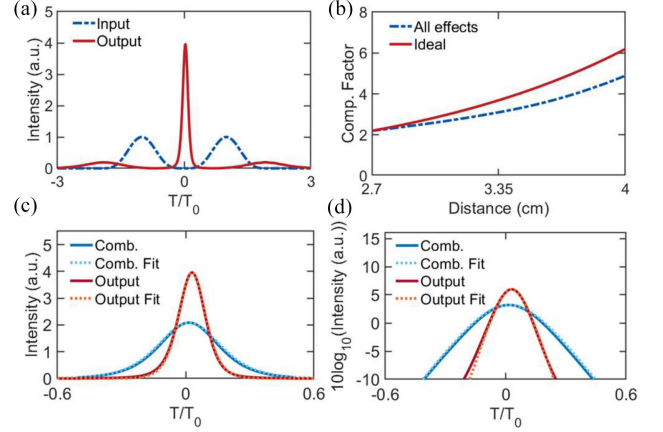


Fig. 7. Numerical simulations of two pulses combination and compression. (a) The profiles of the two initial RC pulses and the resulting compressed pulse. (b) The curves of the compression factors obtained from the all effects and the ideal results over the final 1.3 cm. The comparison of the combined pulse and the output pulse with their corresponding fitted hyperbolic secant pulses in (c) linear scales and (d) logarithmic scales.

wavelength is multiplexed, and the multiplexed beam undergoes phase modulation by a phase modulator to attain the same chirp profile [59]. In this case, the modulation cycle covers two pulses, which is beneficial to achieve the optimal compression factor [58]. In Fig. 6, two pulses combination and compression consist of three main stages of rapid combination, steady adjustment, and nearly self-similar pulse compression. As shown in Fig. 6(a), during the rapid combination process, two RC pulse are emerged into a new born pulse after propagating 1 cm, which appears in the temporal center and accompanies with the FWHM of 143 fs. Subsequently, in the steady adjustment process, the new born pulse will continue to evolve into a combined pulse, while the original pulses undergo a transformation into a pedestal. Note that the combination length ($L_{CL}$) is defined as the waveguide distance at which the peak power of the pedestal drops below 10% of the main peak for the combined pulse. In this context, the combination length is calculated as 2.7 cm. As a result, the successful observation of the combined pulse demonstrates nearly self-similar pulse compression with the compression factor of 4.97. In Fig. 6(b), the normalized spectrum distributions are presented that the compressed pulse undergoes spectral broadening and the final spectrum maintains notable symmetry. In contrast to the initial pulse, the spectral peak power of the output pulse experiences a significant decrease since the center frequency energy is transferred to generate other frequency components.

The numerical simulations of two pulses combination and compression is illustrated in the Fig. 7. As depicted in Fig. 7(a), the temporal profiles of the input and output pulses are observed in linear logarithmic scales. Here, the initial pulse width undergoes compression from 200 fs to 40.2 fs, resulting in the compression factor of 4.97 and the peak power ratio of 3.96. In Fig. 7(b), the two compression factor curves exhibit a similar trend. However, the compression factor considering all effects is 4.97, while the ideal compression factor could be calculated as 6.10 which is derived from the analytical expression of self-similar pulse compression. In Fig. 7(c) and (d), the

combined pulse and the compressed pulse perfectly retain the characteristics of hyperbolic secant pulses in both linear and logarithmic scales. The determined combination length is 2.7 cm that the pulse width declines from 200 fs to 91.2 fs that the initial linear chirp plays a crucial role.

## IV. CONCLUSION

In this article, we demonstrate a theoretical exploration of nearly self-similar pulse compression in the Si-Si$_3$N$_4$ HSWs, which is operating at the wavelength of 2.0 $\mu$m. To extend the self-similar theory beyond single pulse scenarios, our proposed schemes has revealed that both single sech pulse and multiple raised cosine pulses can successfully achieve nearly self-similar pulse compression within the same waveguide. Those results highlight a unique evolutionary process in the compression dynamics. For the single pulse compression, the pulse width reduces from 1 ps to 82.6 fs with the compression factor of 12.11, which is approximately consistent with the mathematical predictions derived from the PPEs method. Furthermore, we employ the Si-Si$_3$N$_4$ HSWs to implement the pulse train compression, where the input pulses are compressed from 2.2 ps to 72 fs with the compression factor of 30.56. Our findings also illustrate that two pulses combination and compression can be realized with the compression factor of 4.97. The Si-Si$_3$N$_4$ HSWs exhibit the capability to achieve nearly self-similar pulse compression from single input pulse to multiple input pulses.

## REFERENCES

[1] M. Yu et al., "Integrated femtosecond pulse generator on thin-film lithium niobate," *Nature*, vol. 612, no. 7939, pp. 252–258, 2022.

[2] D. R. Carlson et al., "Ultrafast electro-optic light with subcycle control," *Science*, vol. 361, no. 6409, pp. 1358–1363, 2018.

[3] T. Ideguchi et al., "Coherent Raman spectro-imaging with laser frequency combs," *Nature*, vol. 502, no. 7471, pp. 355–358, 2013.

[4] E. Obrzud, S. Lecomte, and T. Herr, "Temporal solitons in microresonators driven by optical pulses," *Nature Photon.*, vol. 11, no. 9, pp. 600–607, 2017.

[5] P. L. McMahon et al., "A fully programmable 100-spin coherent Ising machine with all-to-all connections," *Science*, vol. 354, no. 6312, pp. 614–617, 2016.

[6] Q. Guo et al., "Ultrafast mode-locked laser in nanophotonic lithium niobate," *Science*, vol. 382, no. 6671, pp. 708–713, 2023.

[7] A. Blanco-Redondo et al., "Observation of soliton compression in silicon photonic crystals," *Nature Commun.*, vol. 5, no. 1, 2014, Art. no. 3160.

[8] C. Mei et al., "Self-similar propagation and compression of the parabolic pulse in silicon waveguide," *J. Lightw. Technol.*, vol. 37, no. 9, pp. 1990–1999, May 2019.

[9] R. Oliver et al., "Soliton-effect compression of picosecond pulses on a photonic chip," *Opt. Lett.*, vol. 46, no. 18, pp. 4706–4709, 2021.

[10] E. Sahin et al., "Bragg soliton compression and fission on CMOS-compatible ultra-silicon-rich nitride," *Laser Photon. Rev.*, vol. 13, no. 8, 2019, Art. no. 1900114.

[11] J. W. Choi et al., "High spectro-temporal compression on a nonlinear CMOS-chip," *Light Sci. Appl.*, vol. 10, no. 1, 2021, Art. no. 130.

[12] X. Sun, J. S. Aitchison, and M. Mojahedi, "Realization of an ultra-compact polarization beam splitter using asymmetric MMI based on silicon nitride /silicon-on-insulator platform," *Opt. Exp.*, vol. 25, no. 7, pp. 8296–8305, 2017.

[13] Y. Liu et al., "Polarization beam splitter based on a silicon nitride–silica–silicon horizontal slot waveguide," *Opt. Lett.*, vol. 44, no. 6, pp. 1335–1338, 2019.

[14] M. A. Ettabib et al., "Waveguide enhanced raman spectroscopy for biosensing: A review," *ACS Sensors*, vol. 6, no. 6, pp. 2025–2045, 2021.

[15] P. Wang et al., "Design and fabrication of a SiN-Si dual-layer optical phased array chip," *Photon. Res.*, vol. 8, no. 6, 2020, Art. no. 912.

[16] S. Ummethala et al., "Hybrid electro-optic modulator combining silicon photonic slot waveguides with high-k radio-frequency slotlines," *Optica*, vol. 8, no. 4, pp. 511–519, 2021.

[17] W. D. Sacher et al., "Monolithically integrated multilayer silicon nitride-on-silicon waveguide platforms for 3-D photonic circuits and devices," *Proc. IEEE*, vol. 106, no. 12, pp. 2232–2245, Dec. 2018.

[18] Q. Wang et al., "Silicon nitride assisted 1 × 64 optical phased array based on a SOI platform," *Opt. Exp.*, vol. 29, no. 7, pp. 10509–10517, 2021.

[19] Y. Yue, L. Zhang, J. - Y. Yang, R. G. Beausoleil, and A. E. Willner, "Silicon-on-insulator polarization splitter using two horizontally slotted waveguides," *Opt. Lett.*, vol. 35, no. 9, pp. 1364–1366, 2010.

[20] Y. Yue, L. Zhang, H. Huang, R. G. Beausoleil, and A. E. Willner, "Silicon-on-nitride waveguide with ultralow dispersion over an octave-spanning mid-infrared wavelength range," *IEEE Photon. J.*, vol. 4, no. 1, pp. 126–132, Dec. 2012.

[21] C. Mei, "High degree picosecond pulse compression in chalcogenide-silicon slot waveguide taper," *J. Lightw. Technol.*, vol. 34, no. 16, pp. 3843–3852, Aug. 2016.

[22] J. Yuan et al., "Mid-infrared self-similar compression of picosecond pulse in an inversely tapered silicon ridge waveguide," *Opt. Exp.*, vol. 25, no. 26, pp. 33439–33450, 2017.

[23] J. Huang, M. S. A. Gandhi, and Q. Li, "Self-similar chirped pulse compression in the tapered silicon ridge slot waveguide," *IEEE J. Sel. Topics Quantum Electron.*, vol. 26, no. 2, Mar./Apr. 2020, Art. no. 8300508.

[24] C. Mei, D. Wu, T. Feng, X. Zhou, and J. Yuan, "Investigation of multimode self-similar pulse compression in tapered photonic crystal fibers," *J. Lightw. Technol.*, vol. 41, no. 18, pp. 6033–6042, Sep. 2023.

[25] J. Huang, F. Ye, and Q. Li, "Simultaneous pulse combination and nearly self-similar pulse compression in tapered silicon waveguides at around 2.0 $\mu$m," *IEEE Photon. J.*, vol. 14, no. 4, Aug. 2022, Art. no. 3035607.

[26] J. D. Moores, "Nonlinear compression of chirped solitary waves with and without phase modulation," *Opt. Lett.*, vol. 21, no. 8, pp. 555–557, 1996.

[27] J. Ma, Z. Qin, G. Xie, L. Qian, and D. Tang, "Review of mid-infrared mode-locked laser sources in the 2.0 $\mu$m-3.5 $\mu$m spectral region," *Appl. Phys. Rev.*, vol. 6, no. 2, 2019, Art. no. 021317.

[28] A. D. Bristow, N. Rotenberg, and H. M. van Driel, "Two-photon absorption and Kerr coefficients of silicon for 850–2200nm," *Appl. Phys. Lett.*, vol. 90, no. 19, 2007, Art. no. 191104.

[29] F. Leo et al., "Dispersive wave emission and supercontinuum generation in a silicon wire waveguide pumped around the 1550 nm telecommunication wavelength," *Opt. Lett.*, vol. 39, no. 12, pp. 3623–3626, 2014.

[30] H. Saghaei and V. Van, "Broadband mid-infrared supercontinuum generation in dispersion-engineered silicon-on-insulator waveguide," *J. Opt. Soc. Amer. B*, vol. 36, no. 2, 2019, Art. no. A193.

[31] R. K. W. Lau et al., "Octave-spanning mid-infrared supercontinuum generation in silicon nanowaveguides," *Opt. Lett.*, vol. 39, no. 15, pp. 4518–4521, 2014.

[32] B. Kuyken et al., "An octave-spanning mid-infrared frequency comb generated in a silicon nanophotonic wire waveguide," *Nature Commun.*, vol. 6, no. 1, 2015, Art. no. 6310.

[33] X. Gai et al., "Nonlinear absorption and refraction in crystalline silicon in the mid-infrared," *Laser Photon. Rev.*, vol. 7, no. 6, pp. 1054–1064, 2013.

[34] L. Yin and G. P. Agrawal, "Impact of two-photon absorption on self-phase modulation in silicon waveguides," *Opt. Lett.*, vol. 32, no. 14, pp. 2031–2033, 2007.

[35] A. C. Turner-Foster et al., "Ultrashort free-carrier lifetime in low-loss silicon nanowaveguides," *Opt. Exp.*, vol. 18, no. 4, pp. 3582–3591, 2010.

[36] Y. Wang et al., "Enhanced optical nonlinearity in a silicon–organic hybrid slot waveguide for all-optical signal processing," *Photon. Res.*, vol. 10, no. 1, pp. 50–58, 2022.

[37] K. Ikeda, R. E. Saperstein, N. Alic, and Y. Fainman, "Thermal and Kerr nonlinear properties of plasma-deposited silicon nitride/silicon dioxide waveguides," *Opt. Exp.*, vol. 16, no. 17, pp. 12987–12994, 2008.

[38] H. Zhao et al., "Visible-to-near-infrared octave spanning supercontinuum generation in a silicon nitride waveguide," *Opt. Lett.*, vol. 40, no. 10, pp. 2177–2180, 2015.

[39] A. Dhakal et al., "Evanescent excitation and collection of spontaneous Raman spectra using silicon nitride nanophotonic waveguides," *Opt. Lett.*, vol. 39, no. 13, pp. 4025–4028, 2014.

[40] A. Dhakal et al., "Silicon-nitride waveguides for on-chip Raman spectroscopy," *Proc. SPIE*, vol. 9141, 2014, Art. no. 91411C.

[41] L. Zhang et al., "Flat and low dispersion in highly nonlinear slot waveguides," *Opt. Exp.*, vol. 18, no. 12, pp. 13187–13193, 2010.

[42] L. Zhang et al., "On-chip two-octave supercontinuum generation by enhancing self-steepening of optical pulses," *Opt. Exp.*, vol. 19, no. 12, pp. 11584–11590, 2011.

[43] Y. Fang et al., "Recent progress of supercontinuum generation in nanophotonic waveguides," *Laser Photon. Rev.*, vol. 17, no. 1, 2023, Art. no. 2200205.

[44] Y. Fang et al., "Multiple coherent dispersive waves generation in silicon nitride slot waveguide," *Appl. Phys. Lett.*, vol. 120, no. 7, 2022, Art. no. 071103.

[45] L. Xu, M. Yang, Y. Guo, H. Liu, G. Li, and L. Zhang, "Ultrafast pulse manipulation in dispersion-flattened waveguides with four zero-dispersion wavelengths," *J. Lightw. Technol.*, vol. 37, no. 24, pp. 6174–6182, Dec. 2019.

[46] D. J. Blumenthal, R. Heideman, D. Geuzebroek, A. Leinse, and C. Roelofzen, "Silicon nitride in silicon photonics," *Proc. IEEE*, vol. 106, no. 12, pp. 2209–2231, Dec. 2018.

[47] L. Zhang, A. M. Agarwal, L. C. Kimerling, and J. Michel, "Nonlinear group IV photonics based on silicon and germanium: From near-infrared to mid-infrared," *Nanophotonics*, vol. 3, no. 4–5, pp. 247–268, 2014.

[48] H. H. Li, "Refractive index of silicon and germanium and its wavelength and temperature derivatives," *J. Phys. Chem. Reference Data*, vol. 9, no. 3, pp. 561–658, 1980.

[49] I. H. Malitson, "Interspecimen comparison of the refractive index of fused silica," *J. Opt. Soc. Amer.*, vol. 55, no. 10, pp. 1205–1209, 1965.

[50] K. Luke, Y. Okawachi, M. R. E. Lamont, A. L. Gaeta, and M. Lipson, "Broadband mid-infrared frequency comb generation in a Si3N4 microresonator," *Opt. Lett.*, vol. 40, no. 21, pp. 4823–4826, 2015.

[51] Q. Li, K. Senthilnathan, K. Nakkeeran, and P. K. A. Wai, "Nearly chirp- and pedestal-free pulse compression in nonlinear fiber Bragg gratings," *J. Opt. Soc. Amer. B*, vol. 26, no. 3, pp. 432–443, 2009.

[52] B. A. Malomed, "Variational methods in nonlinear fiber optics and related fields," in *Proc. Progess Opt.*, 2002, pp. 71–193.

[53] K. Nakkeeran and P. K. A. Wai, "Generalized projection operator method to derive the pulse parameters equations for the nonlinear Schrödinger equation," *Opt. Commun.*, vol. 244, no. 1–6, pp. 377–382, 2005.

[54] P. Tchofo Dinda, A. B. Moubissi, and K. Nakkeeran, "Collective variable theory for optical solitons in fibers," *Phys. Rev. E, Stat. Phys., Plasmas, Fluids, Related Interdiscipl. Topics*, vol. 64, no. 1, 2001, Art. no. 15.

[55] K. Nakkeeran and P. K. A. Wai, "Behavior of different ansätze in the generalized projection operator method," *Chaos, Solitons Fractals*, vol. 31, no. 3, pp. 639–647, 2007.

[56] Q. Li, K. Nakkeeran, and P. K. A. Wai, "Ultrashort pulse train generation using nonlinear optical fibers with exponentially decreasing dispersion," *J. Opt. Soc. Amer. B*, vol. 31, no. 8, pp. 1786–1792, 2014.

[57] F. Ye, J. Huang, M. S. A. Gandhi, and Q. Li, "Nearly self-similar pulse compression of high-repetition-rate pulse trains in tapered silicon waveguides," *J. Lightw. Technol.*, vol. 39, no. 14, pp. 4717–4724, Jul. 2021.

[58] J. Huang, Q. Li, Z. Jian, P. K. A. Wai, and K. Nakkeeran, "Combination and compression of multiple pulses with same or different wavelengths," *J. Lightw. Technol.*, vol. 38, no. 24, pp. 6932–6938, Dec. 2020.

[59] Q. Li, Z. Jian, W. Lu, K. Nakkeeran, K. Senthilnathan, and P. K. A. Wai, "Combination and compression of multiple optical pulses in nonlinear fibers with the exponentially decreasing dispersion," *IEEE J. Quantum Electron.*, vol. 54, no. 2, Apr. 2018, Art. no. 6800110.